Editors' Suggestion

Broadband high-precision measurement of two-level-system loss using multiwavelength superconducting resonators

Cliff Chen,* Shahriar Aghaeimeibodi, Yuki Sato, Matthew H. Matheny, Oskar Painter, and Jiansong Gao

AWS Center for Quantum Computing, Pasadena, California 91106, USA

(Received 12 June 2025; revised 24 September 2025; accepted 16 December 2025; published 20 January 2026)

Two-level systems (TLSs) are known to be a dominant source of dissipation and decoherence in superconducting qubits. Superconducting resonators provide a convenient way to study TLS-induced loss due to easier design and fabrication in comparison with devices that include nonlinear elements such as Josephson junctions. However, precisely measuring TLS-induced loss in a resonator in the quantum regime is challenging due to low signal-to-noise ratio (SNR) and the temporal fluctuations of the TLS, leading to uncertainties of 20% or more in the loss measurement. To address these limitations, we develop a multiwavelength resonator device that extends the resonator length from a standard quarter wavelength $\lambda/4$ to $N\lambda/4$, where $N = 37$, at 6 GHz. This design provides two key advantages: the TLS-induced fluctuations are reduced by a factor of $\sqrt{N}$ due to spatial averaging over an increased number of independent TLSs, and the measurement SNR for a given intraresonator energy density increases by a factor of $\sqrt{N}$. The multiwavelength resonator also has fundamental and harmonic resonances spanning a wide frequency range, allowing one to study the frequency dependence of TLS-induced loss. In this work we fabricate both multiwavelength and quarter-wave coplanar waveguide resonators formed from thin-film aluminum on a silicon substrate, and characterize their TLS properties at 10 and 200 mK. Our results show that the power-dependent TLS-induced loss measured from the $N\lambda/4$ resonator agrees well with that measured from the $\lambda/4$ resonator, while achieving a fivefold reduction in measurement uncertainty due to TLS fluctuations, down to 5%. The $N\lambda/4$ resonator also provides a measure of the fully unsaturated TLS-induced loss due to the increased measurement SNR at low intraresonator energy densities. Finally, measurements across seven harmonic resonances of the $N\lambda/4$ resonator between 4 and 6.5 GHz reveal no frequency dependence in the TLS-induced loss over this range. These results highlight the benefits of the multiwavelength resonator approach for material development in superconducting quantum circuits.

DOI: 10.1103/2l7h-zn9s

I. INTRODUCTION

Superconducting qubits are among the most promising platforms for scalable quantum computing due to their compatibility with semiconductor technology [1,2]. Recent advances in quantum error correction experiments highlight the need for high-coherence qubits in order to surpass the threshold for fault-tolerant quantum computation [3,4]. Coherence times have steadily increased over the years in large part due to improved circuit designs that reduce the influence of two-level system (TLS) defects located at the interfaces between the substrate, metal, and air [5–10]. These defects are generally assumed to couple the qubit's electric field, and recent advances have focused on reducing this coupling either through optimized design of the qubit capacitor or through the choice of superconducting thin films with lower surface-interface defect density and corresponding loss tangent [5,11,12].

Superconducting resonators are a popular way to assess this TLS-induced loss due to their simpler fabrication and measurement requirements [13]. However, precise measurement of TLS-induced loss in resonators often faces two major challenges. The first challenge is related to the limited drive power one can use to measure the unsaturated resonator loss. Two-level systems are saturable absorbers, and for resonators of small volume such as in planar circuits, in which TLSs couple relatively strongly to the internal resonator electromagnetic field, one must measure resonator loss at low intraresonator photon number, which

*Contact author: clfchen@amazon.com

in many cases is at or below the single-photon limit. Measurement of high-Q microwave resonators at the single-photon level requires the use of an amplifier, the noise of which sets the attainable signal-to-noise ratio (SNR). Ultralow-noise microwave amplifiers, such as cryogenically cooled high electron mobility transistor amplifiers or quantum-limited parametric amplifiers [14], are typically used to boost the SNR. More efficient measurement protocols, such as in Ref. [15], can also aid in reducing the measurement time. Despite these efforts, measuring the unsaturated TLS absorption in high-Q resonators with high accuracy below the single-photon level remains a challenge.

The second, more pernicious challenge is how to address temporal fluctuations in the TLS-induced resonator absorption loss [16]. This phenomenon can be explained by the following simplified model. The drive tone f_r of a resonator interacts with a group of near-resonant TLSs whose transition frequencies $f_{\rm TLS}$ fall within a window $f_r \pm \delta f$, where δf is on the order of the spectral linewidth of the TLS. We can estimate δf to be around 1 MHz, corresponding to the TLS dephasing rate $(1/T_2)$ at the millikelvin temperatures typically used for operation of microwave superconducting quantum circuits [9]. Crucially, the number of TLSs within this $\delta f \approx 1$ MHz interaction zone is not constant in time. Instead, TLS-TLS interactions can cause TLS transition frequencies to drift in and out of this zone, either continuously [17] or abruptly (like a telegraph process [18]). The fluctuating number of TLSs within this $f_r \pm \delta f$ frequency window leads to fluctuations in the TLS absorbed power. Limited by this phenomenon, measurements of TLS-induced absorption loss in quarter-wave (QW) resonators in the single-photon regime often show uncertainties and fluctuations of more than 30% of their mean value [19–21].

To reduce the impact of TLS fluctuations on the loss measurement, we propose using multiwavelength (MW) superconducting resonators. By extending the resonator length from a quarter wavelength ($\lambda/4$) to $N/4$ wavelengths ($N\lambda/4$), we effectively increase the number of TLSs interacting with the microwave tone by a factor of N. As a result, the multiwavelength resonator design reduces the root-mean-square (rms) TLS-induced fluctuations in the measurement result by a factor of $\sqrt{N}$ in comparison with a quarter-wave resonator. The longer resonator length also results in lower energy density in the resonator for a given input power. As the absorption rate of any given TLS is proportional to the local electric field intensity, this allows one to measure the TLS-induced loss down to lower TLS saturation levels ($1/N$) without degrading the measurement SNR (i.e., same input power levels). Finally, the multiwavelength resonator exhibits fundamental and harmonic resonances across a wide frequency range that enables broadband studies of frequency-dependent TLS loss.

II. DEVICE PRINCIPLE

We explain the principle of the multiwavelength resonator design by comparing it with a standard transmission-line quarter-wave resonator, as illustrated in Fig. 1, which shows circuit diagrams of both a quarter-wave resonator [Fig. 1(a)] and a multiwavelength resonator [Fig. 1(b)], each coupled to a feedline that connects to a cryogenic amplifier. Consider exciting the $\lambda/4$ resonator by a microwave tone of power P_f on the feedline, which results in an average of $n_{{\rm ph},\lambda/4}$ photons stored in the resonator. Its local electric field distribution is given by

$$\vec{E}(x,y,z) = \vec{E}_0(x,y)\cos\left(\frac{2\pi z}{\lambda}\right), \quad (1)$$

where $\vec{E}_0(x,y)$ represents the electric field distribution in the x-y cross section, and z ranges from 0 to $l = \lambda/4$, with $z = 0$ representing the open end. For a coplanar waveguide (CPW) resonator, $E_0(x,y)$ corresponds to the TEM mode of the CPW, which can be determined by solving a two-dimensional electrostatic problem. A multiwavelength resonator's electric field distribution maintains the

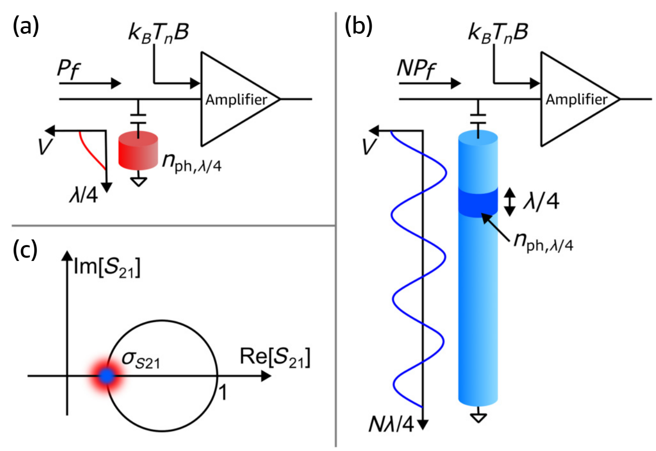

FIG. 1. $\lambda/4$ and $N\lambda/4$ resonators. (a) A quarter-wave resonator coupled to a feedline with an amplifier. The resonator is driven with probe power $P_f^{\rm QW}$, and the output signal is read out through the amplifier, with noise temperature T_n over the measurement bandwidth B. (b) A multiwavelength ($N\lambda/4$) resonator coupled to a feedline operating at the same resonance frequency and with the same amplifier as the $\lambda/4$ resonator in (a). The probe power $P_f^{\rm MW}$ in in this case is $NP_f^{\rm QW}$, so each $\lambda/4$ section of the multiwavelength resonator has the same number of photons $n_{{\rm ph},\lambda/4}$ as the quarter-wave resonator. (c) Measurement of S_{21} of the quarter-wave and multiwavelength resonators in (a),(b) would yield the same normalized resonance circle. However, the S_{21} measurement uncertainty $\sigma_{S_{21}}$ would be a factor of $\sqrt{N}$ smaller for the multiwavelength resonator (blue circle) in comparison with the quarter-wave resonator (red circle). Here we assume the S_{21} uncertainty is dominated by the amplifier noise, so it is given as $\sigma_{S_{21}} \approx \sqrt{k_BT_nB/P_f}$.

same form as Eq. (1), but with z extending from $l = 0$ to $l = N\lambda/4$, where N is the number of quarter wavelengths. Importantly, the TLSs couple to the local electric field through their dipole moments, which requires $E^{\mathrm{MW}}(x,y) = E^{\mathrm{QW}}(x,y)$ in order to have the same TLS-induced loss per unit length. We refer to this requirement as the "equal electric field condition." Under this condition, each $\lambda/4$ segment of the MW resonator stores an average of $n_{\mathrm{ph},\lambda/4}$ photons, matching the QW resonator, and the total number of photons is expressed as $n_{\mathrm{ph},\lambda/4} = N n_{\mathrm{ph},\lambda/4}$ because there are N segments. Henceforth, we refer to $n_{\mathrm{ph},\lambda/4}$ as the "photon density," representing the number of photons per unit $\lambda/4$ section of the resonator, and n_{ph} as the "total number of intraresonator photons."

Now we turn to analyzing the TLS-induced loss in a resonator following the model in Ref. [22]. The TLSs are assumed to be uniformly distributed within a volume V_h, which occupies a portion of the total resonator volume V. These TLSs contribute to the complex dielectric constant $\epsilon_{\mathrm{TLS}} = \epsilon_1 - j\epsilon_2$ and loss tangent $\delta_{\mathrm{TLS}} = \epsilon_2/\epsilon_1$. The mean value of the TLS-induced resonator loss $\xi = 1/Q_{\mathrm{TLS}}$ is given as

$$\xi = \frac{\int_{V_h} \epsilon_2 |\vec{E}|^2 d\vec{r}}{\int_V \epsilon |\vec{E}|^2 \, d\vec{r}} = F\delta_{\mathrm{TLS}}, \quad F = \frac{\iint_{\Omega_h} \epsilon |\vec{E}_0|^2 \, dx\, dy}{\iint_{\Omega} \epsilon |\vec{E}_0|^2 \, dx\, dy}, \tag{2}$$

where ϵ is the real part of the dielectric constant, while Ω_h and Ω represent the TLS occupied area and the total area in the resonator's x-y cross section, respectively. F is theTLS filling factor and represents the fraction of the resonator's total electrical energy stored in the TLS-hosting material. In the derivation of Eq. (2), we used the electric field distribution from Eq. (1). Since δ_{TLS} and F are independent of the resonator length l and the number of quarter wavelengths N, measurements performed on $\lambda/4$ and $N\lambda/4$ resonators should yield identical results for ξ. Furthermore, according to the standard tunneling TLS model [17], the TLS loss tangent can saturate with temperature and electric field strength, resulting in a power-dependent and temperature-dependent ξ expressed as

$$\xi = \xi_0 \frac{\tanh\left(\frac{\hbar\omega}{2k_B T}\right)}{\sqrt{1 + (|\vec{E}|/E_c)^2}}, \quad \xi_0 = F\delta^0_{\mathrm{TLS}}, \tag{3}$$

where ω is the angular frequency of the probe tone, k_B is the Boltzmann constant, T is the resonator temperature, δ^0_{TLS} is the intrinsic TLS loss tangent, and E_c is the characteristic electric field strength for TLS saturation. This means that ξ_0 is an intrinsic property of the resonator that depends on its geometry and material composition, but is independent of power and temperature; therefore, it serves as an important figure of merit for comparing different resonator designs and materials.

Next we consider fluctuations in ξ. If the TLS-induced dielectric constant fluctuates on timescales that are much longer than the resonator's period, one would expect to see ξ fluctuations given by

$$\delta\xi(t) = \frac{\int_{V_h} \delta\epsilon_2(\vec{r},t) |\vec{E}|^2 \, d\vec{r}}{\int_V \epsilon |\vec{E}|^2 \, d\vec{r}}. \tag{4}$$

To proceed, we make some assumptions about the correlation function $\langle \delta\epsilon_2(\vec{r}_1,t_1)\delta\epsilon_2(\vec{r}_2,t_2)\rangle$ between two regions of ϵ_2. For independently fluctuating TLSs, we expect, under the assumption of stationarity, that the correlation function has the form $\langle \delta\epsilon_2(\vec{r}_1,t_1)\delta\epsilon_2(\vec{r}_2,t_2)\rangle = C(\vec{r}_1, t_1 - t_2)\delta(\vec{r}_1 - \vec{r}_2)$, where $C(\vec{r}_1, t_1 - t_2)$ is some function of a single position coordinate and only the time difference. Furthermore, because the TLSs are also assumed to be uniformly distributed in V_h, we expect $C(\vec{r}_1, t_1 - t_2)$ to be independent of position $\vec{r}_1$, which allows it to be rewritten as $C(t_1 - t_2)$. We can now derive the correlation function of the ξ fluctuations as [22]

$$\langle \delta\xi(t)\delta\xi(0)\rangle = \frac{C(t)\int_{V_h} |\vec{E}|^4 \, d\vec{r}}{\left(\int_V \epsilon |\vec{E}|^2 \, d\vec{r}\right)^2} = C(t)\rho_{xy}\rho_z, \tag{5}$$

where we have used Eq. (1) and the assumption that the TLS distribution is z independent to write the result as a product of two terms, ρ_{xy} and ρ_z. The first term

$$\rho_{xy} = \frac{\iint_{\Omega_h} |\vec{E}_0|^4 \, dx\, dy}{\left(\iint_{\Omega} \epsilon |\vec{E}_0|^2 \, dx\, dy\right)^2} \tag{6}$$

involves only integrals in the x-y plane and is therefore the same for QW and MW resonators under the equal electric field condition. The second term involves only integrals of z, which we evaluate to be

$$\rho_z = \frac{\int_0^{N\lambda/4} \cos^4(\frac{2\pi z}{\lambda}) \, dz}{\left(\int_0^{N\lambda/4} \cos^2(\frac{2\pi z}{\lambda}) \, dz\right)^2} = \frac{6}{N\lambda}, \quad N = 1, 3, 5, 7, \ldots. \tag{7}$$

Because of N in the denominator, the correlation function is reduced by a factor of N in a MW resonator compared with a QW resonator. By taking $t = 0$ in Eq. (5), we arrive at

$$\langle \delta\xi^2\rangle^{\mathrm{MW}} = \langle \delta\xi^2\rangle^{\mathrm{QW}}/N, \tag{8}$$

thus demonstrating the N-fold reduction in the variance $\langle \delta\xi^2\rangle$ of the TLS-induced loss. It follows from the assumption of stationarity and the Wiener-Khinchin theorem that the power spectral density (PSD) of ξ fluctuations S_ξ will have the same relationship:

$$S_\xi^{\mathrm{MW}}(\nu) = S_\xi^{\mathrm{QW}}(\nu)/N. \tag{9}$$

In addition to reducing the intrinsic TLS-induced fluctuations in ξ, a MW resonator has the advantage that it can also increase the measurement SNR for a given level of TLS saturation. Assuming the equal electric field condition (i.e., equal TLS saturation), equal coupling Q_c, equal resonance frequencies ($f_{r,N}^{\mathrm{MW}} = f_{r,1}^{\mathrm{QW}}$), and that the internal Q_i is limited by Q_{TLS}, the two types of resonators should have the same Q_i and loaded Q. This indicates that an S_{21} measurement of both resonators would yield the same resonance circle. However, the probe power P_f used to measure the $N\lambda/4$ resonator would be N times greater, $P_f^{\mathrm{MW}} = NP_f^{\mathrm{QW}}$, despite the same S_{21} response. This follows from the fact that the equal electric field condition is equivalent to having the same internal microwave power P_{int}, where $P_{\mathrm{int}} = (2/N\pi)(Q^2/Q_c)P_f$ [22]. Therefore, assuming we have the same amplifier noise level, the S_{21} measurement uncertainty $\sigma_{S_{21}}$ is expected to be a factor of $\sqrt{N}$ smaller for the MW resonator in comparison with the QW resonator, as we show in Fig. 1(c). Conversely, this implies that when $P_f^{\mathrm{MW}} = P_f^{\mathrm{QW}}$, $E^{\mathrm{MW}}(x,y) \sim E^{\mathrm{QW}}(x,y)/\sqrt{N}$. This indicates that the MW resonator can reduce the intraresonator energy density $|E(x,y)|^2$ by a factor of$N$ while maintaining a similar SNR as that of a QW resonator, thus making observation of ξ_0 easier. As a summary of this section, we list the relationships between the MW and QW versions of various parameters in Eqs. (10a) and (10b):

$$\begin{aligned} \vec{E}^{\mathrm{MW}} &= \vec{E}^{\mathrm{QW}}, \\ f_{r,N}^{\mathrm{MW}} &= f_{r,1}^{\mathrm{QW}}, \\ Q_c^{\mathrm{MW}} &= Q_c^{\mathrm{QW}} \end{aligned} \tag{10a}$$

implies the following

$$\begin{aligned} n_{\mathrm{ph}}^{\mathrm{MW}} &= Nn_{\mathrm{ph}}^{\mathrm{QW}}, \\ n_{\mathrm{ph}}^{\mathrm{MW}} &= n_{\mathrm{ph}}^{\mathrm{QW}}, \\ P_f^{\mathrm{MW}} &= NP_f^{\mathrm{QW}}, \\ \langle \delta\xi^2 \rangle^{\mathrm{MW}} &= \langle \delta\xi^2 \rangle^{\mathrm{QW}}/N, \\ S_\xi^{\mathrm{MW}} &= S_\xi^{\mathrm{QW}}/N, \\ [\sigma_{S_{21}}^2]^{\mathrm{MW}} &= [\sigma_{S_{21}}^2]^{\mathrm{QW}}/N. \end{aligned} \tag{10b}$$

III. DEVICE FABRICATION AND EXPERIMENTAL SETUP

To compare the performance of the $N\lambda/4$ design against that of the standard $\lambda/4$ design, we fabricated two devices

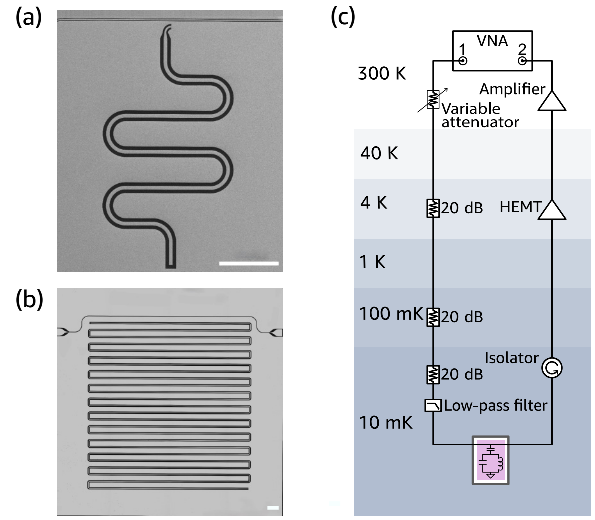

FIG. 2. Devices and experimental setup. (a) Scanning electron micrograph of the $\lambda/4$ resonator design. (b) False-color optical micrograph of the $N\lambda/4$ resonator design. (c) Measurement setup used in this study. White scale bars at the bottom right in (a),(b) correspond to 500 µm.

from a 100-nm-thick Al film deposited on a high-resistivity (approximately 10 kΩ cm) silicon substrate (see Appendix A). One device contained 11 hanger-style $\lambda/4$ resonators of different lengths (5.45–5.67 mm) coupled to a common transmission line, while the other contained a single $N\lambda/4$ resonator (181 mm) with a fundamental frequency of 165 MHz, as shown in Figs. 2(a) and 2(b) (see Appendix B). Both resonator designs used a CPW geometry with a 30 µm center strip and 30 µm gap widths. We chose adjacent dies for each device in order to help eliminate spatial variations during fabrication.

The devices were cooled in a dilution refrigerator, and S_{21} measurements on each device were performed with a vector network analyzer (VNA) in the setup shown in Fig. 2(c). To best utilize the measurement time, we implemented the hybrid approach of parameter-constrained conformal mapping method as described in Ref. [15] (see Appendix C). At high powers ($n_{\mathrm{ph},\lambda/4} \gtrsim 10^4$) in the linear regime, we performed frequency sweeps of the S_{21} measurement centered at $f = f_r$ and extracted the loss along with power-independent resonator parameters by fitting the data using the diameter correction method [23]; the error bars represent the 1σ confidence interval. At lower powers, we measured the time-dependent $S_{21}(f, t)$ on resonance at a single frequency $f = f_r$ for a few seconds. We then conformally mapped the $S_{21}(f_r, t)$ time series into $1/Q_i(t)$ using the power-independent parameters determined at high power to obtain the average $1/Q_i$ value at each lower power [15]; in this case, the error bars represent the standard error of the mean. Finally, the TLS-induced loss was obtained by subtraction of the power-independent loss component ($1/Q_{i,\mathrm{HP}}$, measured at highest power) from the total resonator loss ($1/Q_i$), yielding $\xi = 1/Q_{\mathrm{TLS}} = 1/Q_i - 1/Q_{i,\mathrm{HP}}$.

IV. RESULTS

A. Comparison of ξ versus $n_{\mathrm{ph},\lambda/4}$ for multiwavelength and quarter-wave resonators

We experimentally compare the power-dependent TLS loss ξ measured from the $N\lambda/4$ and $\lambda/4$ resonators in Fig. 3; the lowest microwave power used was around -165 dBm ($n_{\mathrm{ph},\lambda/4} \sim 0.0002$), with each curve taken 5 min apart from each other. Measurements were first performed at the base temperature (10 mK) of the dilution fridge. The loss curves from the $\lambda/4$ resonators (red) and the $N\lambda/4$ resonator (blue), with $27 \leq N \leq 39$, lie roughly on top of each other when plotted against photon density $n_{\mathrm{ph},\lambda/4}$. This overlap confirms that both resonator types yield the same measurement result for ξ, as expected given their identical cross-section CPW geometry and fabrication. The average loss ξ across all frequencies at $n_{\mathrm{ph},\lambda/4} \approx 1$ is $(4.66 \pm 0.49) \times 10^{-7}$ for the $N\lambda/4$ resonator and $(3.96 \pm 0.57) \times 10^{-7}$ for the $\lambda/4$ resonators. Notably, the loss curves do not plateau for either type of resonator even at the lowest power, making it impossible to extract the intrinsic loss $\xi_0 = F\delta_0$.

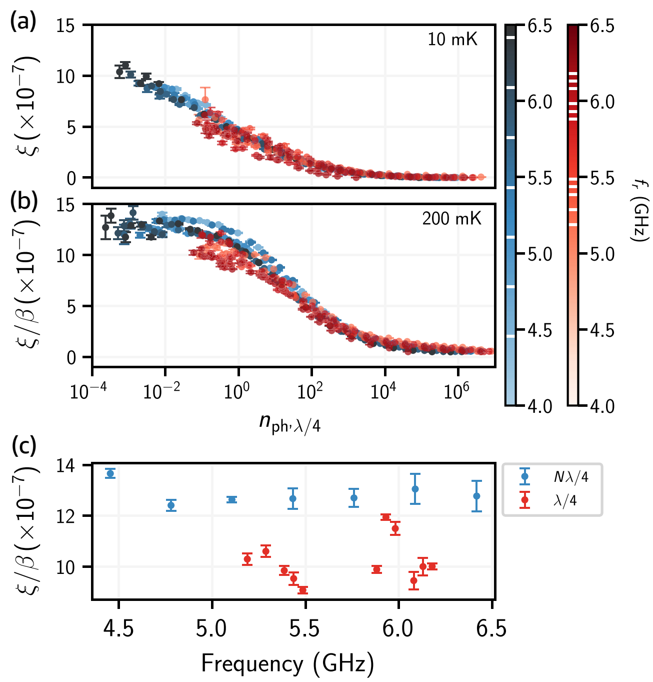

FIG. 3. Measurement of ξ vs $n_{\mathrm{ph},\lambda/4}$ for Al-based $\lambda/4$ and $N\lambda/4$ CPW resonators. (a) ξ vs $n_{\mathrm{ph},\lambda/4}$ measured at 10 mK for 11 $\lambda/4$ resonators (red) and seven $N\lambda/4$ resonances (blue) covering a resonance frequency range of 4–6.5 GHz. Corresponding resonance frequencies for each resonator are indicated by the white marks in the color bar. (b) Temperature-corrected ξ vs $n_{\mathrm{ph},\lambda/4}$ for the same resonators as in (a) measured at 200 mK. The temperature factor $\beta = \tanh(hf_r/2k_BT)$, as defined in Eq. (3), where $T = 0.2$ K, has been divided out. The quasiparticle loss from the elevated temperature has also been removed. (c) Temperature-corrected loss values extracted from (b) at the lowest photon densities plotted against f_r.

To address this issue, we repeated the measurements at a temperature of 200 mK. Raising the temperature extends the plateau region to higher powers by increasing the critical electric field $\vec{E}_c$ that results in TLS saturation. This occurs because the critical electric field scales as $|\vec{E}_c| \propto (T_1T_2)^{-1/2}$, where the relaxation ($1/T_1$) and dephasing ($1/T_2$) rates both increase with temperature [22,24,25]. To remove the temperature-dependent factor [$\beta = \tanh(hf_r/2k_BT)$] from the TLS loss in Eq. (3), we plot in Fig. 3(b) a temperature-corrected loss of ξ/β. The thermal quasiparticle loss associated with the elevated temperature [22,26] has been subtracted and accounted for by the power-independent loss term $1/Q_{i,\mathrm{HF}}$. A distinct plateau region is observed in the $N\lambda/4$ curves at low photon densities ($n_{\mathrm{ph},\lambda/4} < 0.1$), while the $\lambda/4$ curves follow a similar shape but are limited to an N times higher region of $n_{\mathrm{ph},\lambda/4}$ due to the limited SNR at the lowest $n_{\mathrm{ph},\lambda/4}$. Reading directly from this plateau region of the $N\lambda/4$ resonator, where the TLSs are in their ground state, we can safely determine the intrinsic loss parameter $\xi_0 = F\delta^0_{\mathrm{TLS}} = 1.25 \times 10^{-6}$.

In Fig. 3(c), we plot ξ against f_r for each of the resonators. The loss values were extracted from the temperature-corrected 200 mK data at the lowest measured photon density $n_{\mathrm{ph},\lambda/4}$. The $\lambda/4$ resonator loss values (red) are slightly lower (by 15%) than those of the $N\lambda/4$ resonator, primarily because the $\lambda/4$ resonator measurements barely reach the plateau region. We observe no clear frequency dependence of the loss across a span of approximately 2 GHz, with the exception of a slight upturn at 4.5 GHz ($N = 27$). This is mostly consistent with the standard model of a uniform TLS density of states [17,27]. The upturn appears to exceed the 1σ error bars calculated from this short measurement interval, but as we discuss in the next section, additional experiments demonstrate that time-dependent drifts can increase the loss variation by an additional 5%. Further study of the uniformity of the TLS density of states using this MW resonator is required to confirm if the upturn is statistically significant.

B. Comparison of ξ fluctuations measured for multiwavelength and quarter-wave resonators

On the basis of the analysis presented, a MW resonator is expected to show a $\sqrt{N}$-fold reduction in ξ fluctuations compared with a QW resonator when operated at similar resonance frequencies and excited to equivalent photon densities $n_{\mathrm{ph},\lambda/4}$. We experimentally demonstrate this insensitivity to TLS drift on both short (seconds) and long (hours) timescales.

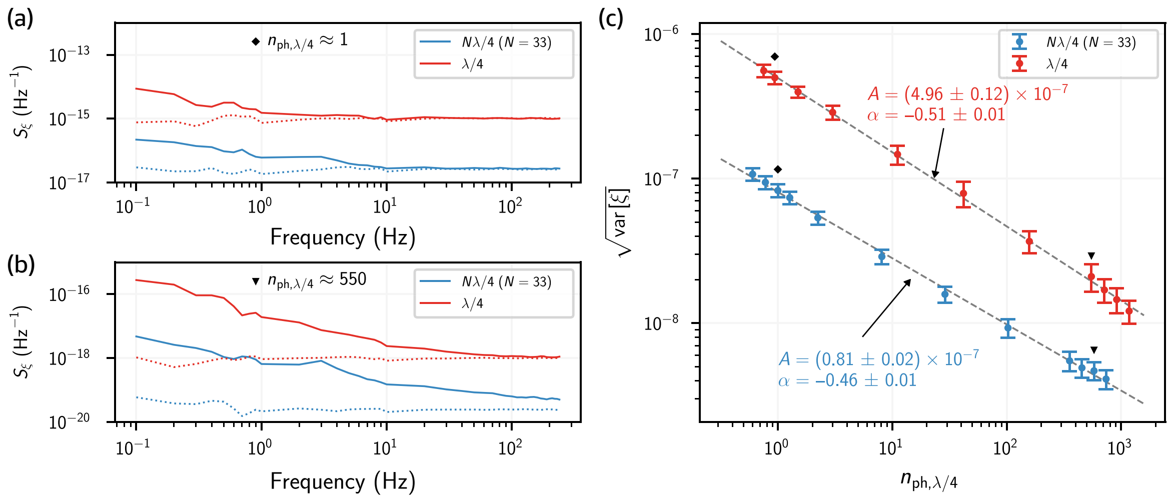

FIG. 4. Power spectral densities and rms fluctuations of ξ vs $n_{\mathrm{ph},\lambda/4}$ for $\lambda/4$ and $N\lambda/4(N = 33)$ resonators measured at 10 mK. (a) Solid lines correspond to the power spectral densities of the data projected along the $\hat{\xi}$ quadrature at $n_{\mathrm{ph},\lambda/4} \approx 1$. Dotted lines correspond to the power spectral densities of the transmission background taken off resonance ($f = f_r + 2$ MHz) after projection. (b) The same as in (a) but for $n_{\mathrm{ph},\lambda/4} \approx 550$. (c) Each point corresponds to data taken on resonance for 100 s at a sampling rate of 500 Hz. The data were subsequently projected along the dissipation quadrature $\hat{\xi}$, from which the PSD was estimated by Welch's method. Next, the variance was calculated by integration of the PSD down to 0.1 Hz. The dashed gray lines indicate best fits to a scaling law of the form $\sqrt{\mathrm{var}[\xi]} = A n_{\mathrm{ph},\lambda/4}{}^{\alpha}$. For the points marked with a black diamond or a black triangle, the corresponding PSDs are shown in (a),(b), respectively.

First, we show the $\sqrt{N}$-fold improvement on a short timescale of 0.1–10 s. Note that on this timescale the noise in the inferred value of ξ is a combination of both the white noise of the amplifier and the low-frequency noise of the TLS frequency fluctuations. We compare the power spectral densities (PSDs) between an $N\lambda/4$ resonator with $N = 33$ (5.43 GHz) and a $\lambda/4$ (5.23 GHz) resonator. The raw data were obtained by measuring the on-resonance time-dependent $S_{21}(f, t)$ at a single frequency $f \approx f_r$ for 100 s at a sample rate of 500 Hz. We subsequently projected the data onto the dissipation quadrature $\hat{\xi}$ and converted it to $\xi(t)$, from which we computed the PSD $S_\xi(\nu)$ using Welch's method [28]. The 100 s length was chosen to reduce the uncertainty in the PSD estimate at low frequencies near 0.1 Hz. This analysis protocol follows standard procedures for characterizing quadrature-dependent resonator noise [22] (see Appendix D).

We plot the resulting $S_\xi(\nu)$ as solid lines in Figs. 4(a) and 4(b) for $n_{\mathrm{ph},\lambda/4} \approx 1$ and $n_{\mathrm{ph},\lambda/4} \approx 550$, respectively. For reference, we also include the system noise floors (dashed lines) measured off resonance at $f = f_r + 2$ MHz. For both resonators, the noise floors appear as white noise that converge with the on-resonance PSDs (solid lines) for $\nu > 10$ Hz. Toward lower frequencies ($\nu < 1$ Hz), $S_\xi(\nu)$ exhibits a $1/f$-noise behavior that rises above the white noise floor (set by the amplifier noise), which suggests that TLS-induced fluctuations are the dominant noise mechanism in this frequency range. As discussed previously, the noise power of both the TLS frequency fluctuations and the amplifier noise is expected to reduce by a factor of N in the MW resonators. Indeed, we observe a large separation between the noise power spectral densities of $S_\xi(\nu)$ throughout the entire frequency range, with the noise power spectral density for the $N\lambda/4$ resonator being more than 30 times lower than that for the $\lambda/4$ resonator. This result demonstrates the effectiveness of the MW resonator design in substantially reducing the ξ fluctuation for short timescales of less than 10 s. The amount of noise power reduction is also in good agreement with the prediction of the factor $N = 33$ [Eq. (9)].

We further demonstrate this reduction over a range of microwave signal powers by plotting the rms fluctuations in ξ, $\sqrt{\mathrm{var}[\xi]}$, against $n_{\mathrm{ph},\lambda/4}$ in Fig. 4(c). Each point is calculated by our integrating its corresponding PSD down to 0.1 Hz. The dotted gray lines correspond to best fits to a scaling law of the form $\sqrt{\mathrm{var}[\xi]} = A n_{\mathrm{ph},\lambda/4}{}^{\alpha}$. We extract an exponent of $\alpha \approx 0.5$ for both resonators. This is expected for fluctuations that are dominated by white noise from the cryogenic amplifier. In this case, the S_{21} uncertainty, and hence the uncertainty in ξ, obeys $\sigma_{S21} \propto 1/\sqrt{P_f} \propto 1/\sqrt{n_{\mathrm{ph},\lambda/4}}$. Comparison of the prefactors indicates that $A_{\lambda/4}/A_{N\lambda/4} = 6.2 \pm 0.2$, showing again a reduction in noise on the order of $\sqrt{N}$ across a wide range of photon densities. We note that the reduction factor of exactly $\sqrt{N}$ is derived under the assumption that both resonators share identical geometry, Q_c, Q, and are excited to produce equivalent electric field strength and distribution $\vec{E}_0(x, y)$. In our case, the Q_c values for the two resonators were chosen to be similar but still differed by 15%. Additionally, imperfection in power calibration and chip-to-chip variations in TLS density may also affect the actual observed $S_\xi(\nu)$ reduction factor.

Next we compare the long-term performance on a timescale of hours. We conducted repeated measurements of ξ versus $n_{\mathrm{ph},\lambda/4}$ curves (similar to those in Fig. 3) at 10 mK over a 12 h period on two $N\lambda/4$ resonators and two $\lambda/4$ resonators with similar resonance frequencies at 5.43 and 6.08 GHz. Each ξ versus $n_{\mathrm{ph},\lambda/4}$ curve took about 2 min (12 power steps with 10 s measurement time at each step) to collect, and a total 100 curves were collected per resonator or resonance. The MW and QW datasets were taken during separate 12 h measurement periods.

We pick 12 random ξ versus $n_{\mathrm{ph},\lambda/4}$ curves from this 12 h period for each resonator type and overlay them in Figs. 5(a) and 5(c). Qualitatively, the MW curves show notably less spread than the $\lambda/4$ curves over the 12 h. For numerical comparison, we calculated the empirical cumulative distribution functions (ECDFs) of the ξ values measured for $n_{\mathrm{ph},\lambda/4} \approx 1$ from the full 100 curve datasets and plot them in Figs. 5(b) and 5(d); the corresponding Dvoretzky-Kiefer-Wolfowitz confidence bands at the 99% level are shown as the filled areas [29]. These ECDFs

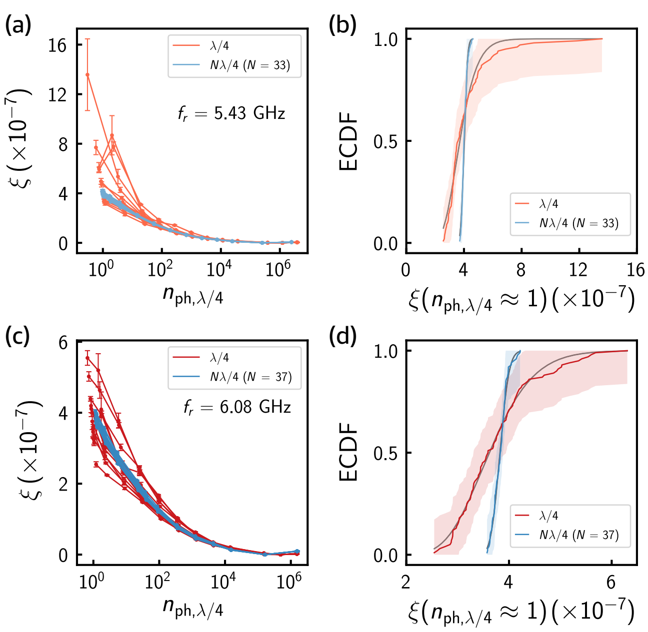

FIG. 5. Repeated ξ measurements for $\lambda/4$ and $N\lambda/4$ resonators at 10 mK over 12 h. (a),(c) The repeated measurements of ξ vs $n_{\mathrm{ph},\lambda/4}$ over 12 h for two $\lambda/4$ resonators (red) and two $N\lambda/4$ resonances (blue) at 5.43 and 6.08 GHz. For clarity, we plot only 12 randomly selected curves out of the total of 100 curves for each resonator. (b),(d) Empirical cumulative distribution functions of $\xi(n_{\mathrm{ph},\lambda/4} \approx 1)$ taken from the 100-curve datasets. Gray lines indicate best fits to a log-normal distribution. The filled areas correspond to the Dvoretzky-Kiefer-Wolfowitz confidence bounds calculated at the 99% confidence level.

TABLE I. Mean $E[\xi]$, variance var$[\xi]$, and relative errors $\sqrt{\mathrm{var}[\xi]}/E[\xi]$ obtained from fitting the empirical cumulative distributions of $\xi_{1\mathrm{ph}}$ in Fig. 5 to a log-normal distribution.

f_r (GHz)	N	$E[\xi]/10^{-7}$	var$[\xi]/10^{-14}$	$\sqrt{\mathrm{var}[\xi]}/E[\xi]$
5.43	1	3.83 ± 0.016	0.968 ± 0.055	0.256
5.43	33	4.018 ± 0.001	0.032 ± 0.0009	0.044
6.08	1	3.677 ± 0.005	0.476 ± 0.012	0.188
6.09	37	3.826 ± 0.001	0.019 ± 0.0005	0.036

were fitted to a log-normal distribution and we found good agreement; the results of the fits are tabulated in Table I (see Appendix E). Compared with their $\lambda/4$ counterparts, the $N\lambda/4$ resonators demonstrate reductions in the rms fluctuation of ξ by factors of 5.5 and 4.9 for $N = 33$ and $N = 37$, respectively. This corresponds to a fivefold decrease in the relative uncertainties of ξ from greater than 20% to less than 5%, which is achieved with a measurement time of only 10 s. The smaller improvement of the $N = 37$ resonator over the corresponding $\lambda/4$ resonator could be attributed to potential intrachip fabrication variations; we observed before that different resonators within the same die can have different levels of loss and fluctuations. These findings further confirm the improved performance of the $N\lambda/4$ design over the standard $\lambda/4$ design, demonstrating reduced ξ fluctuations and greater measurement sensitivity across both short and long timescales.

V. DISCUSSION

The multiwavelength resonator device significantly increases TLS loss measurement sensitivity, enabling us to investigate deep into the sub-single-photon regime. The results shown in Fig. 3 highlight an important distinction between two key quantities, $\xi_{1\mathrm{ph}}$ and ξ_0. $\xi_{1\mathrm{ph}}$ characterizes the TLS loss near $n_{\mathrm{ph},\lambda/4} \approx 1$ and is dependent on circuit operating conditions (such as input power and its proximity to the TLS-saturation power), while ξ_0 represents the intrinsic TLS loss limited by material and circuit design parameters. Importantly, $\xi_{1\mathrm{ph}}$ and ξ_0 can differ due to TLS saturation effects.

In our 10 mK measurements, neither resonator type exhibits a loss plateau at the lowest powers, despite reaching photon densities as low as approximately 10^{-1} in the $\lambda/4$ resonator case and approximately 10^{-3} in the $N\lambda/4$ resonator case. Given the absence of a plateau, ξ_0 cannot be extracted from the 10 mK measurements. Conversely, at an elevated temperature of 200 mK, a distinct plateau emerges in the loss curves, allowing us to precisely determine ξ_0. Notably, $\xi_{1\mathrm{ph}}$ is approximately half the value of ξ_0 in the resonators studied here. This demonstrates that combining temperature control with the MW resonator can provide a more comprehensive characterization of TLS-induced loss and lead to better comparisons between different materials and designs [20,21]. As part of future research, we plan to use this tool to investigate further the geometry and frequency dependence of TLS-induced loss.

We note that the improved precision of the MW resonator comes from its coupling to a large number of TLSs and making use of the central limit theorem; therefore, it is important to check that we are not in the few-TLS limit. We can estimate the number of TLSs within our MW resonator on the basis of TLS densities found in the literature. With a TLS density of $100\,\mathrm{GHz}^{-1}\,\mu\mathrm{m}^{-3}$ [30], we calculate that there are approximately 10^6 TLSs per gigahertz on the center strip of our MW resonator, assuming the TLSs occupy a 2-nm-thick layer. Combined with a typical TLS linewidth of 1 MHz [9], the microwave tone interacts with roughly 10^3 TLSs at any moment. This places our device in a regime where we perform averaging over a large ensemble of TLSs and differs from the case of small-volume devices such as Josephson junctions, where only a few discrete TLSs are involved.

The averaging effect of the MW resonator implies that measuring a single $N\lambda/4$ resonator is, in principle, equivalent to measuring N identical $\lambda/4$ resonators at the same resonance frequency spread out through a single chip. However, the multi-$\lambda/4$-resonator approach is significantly more demanding from a resource standpoint, either requiring more hardware if measurements are parallelized or more time if they are performed sequentially. There are also the added issues of frequency collisions and crosstalk as the number of QW resonators per chip increases, which can be exacerbated by nonuniformity in the fabrication process [31]; both these issues are mitigated in the MW approach. These arguments also apply to measurements of the resonator frequency, in which the stability of the MW approach can enable precise determination of the temperature-dependent frequency shift due to TLSs. We reemphasize that these precision improvements apply only to a single chip; wafer-scale variations can still introduce changes in the loss larger than what is observed here.

Finally, we mention some considerations that should be taken into account when an $N\lambda/4$ resonator is used to probe absorption loss. First, since the coupling quality factor Q_c varies with frequency, the coupling structure must be carefully designed to accommodate the specific frequency band of interest. Second, the larger physical footprint of the resonator means that is is more susceptible to parasitic modes in comparison with the standard $\lambda/4$ resonator. Air bridges or wire bonds should be added to the device to maintain ground plane continuity and suppress unwanted modes.

VI. CONCLUSION

In conclusion, we have shown that a multiwavelength resonator device reduces the TLS-induced loss measurement uncertainty in comparison with conventional quarter-wave resonator devices. Our theoretical and experimental results demonstrate that the multiwavelength resonator reduces fluctuations from both the TLSs in the device and the cryogenic amplifier, resulting in a $\sqrt{N}$ reduction in measurement uncertainty, both on short timescales (seconds) and on long timescales (hours). Additionally, the multiwavelength resonator reduces the photon density in the resonator for a given SNR, enabling more efficient observation of the fully unsaturated TLS contribution to the resonator loss ξ_0. Finally, the multiple resonances of a multiwavelength resonator provide a spectral analysis of the TLS-induced absorption loss. Taken together, these properties of a multiwavelength resonator make it a valuable tool for investigating the impacts of materials, resonator designs, and fabrication processes on quantum device performance.

ACKNOWLEDGMENTS

We thank the staff of the AWS Center for Quantum Computing who enabled this project. We also thank Simone Severini, James Hamilton, Nafea Bshara, and Peter DeSantis for their support of the research activities at the AWS Center for Quantum Computing.

DATA AVAILABILITY

The data that support the findings of this article are openly available [32], embargo periods may apply.

APPENDIX A: DEVICE DESIGN AND FABRICATION

One 1×1 cm^2 quarter-wave device [Fig. 6(a)] and one 1×1 cm^2 multiwavelength device [Fig. 6(b)] were fabricated on the same high-resistivity silicon wafer with 100-nm-thick aluminum deposited on it. All resonators used a coplanar-waveguide geometry with a $30\,\mu$m center strip and $30\,\mu$m gap widths. The quarter-wave device

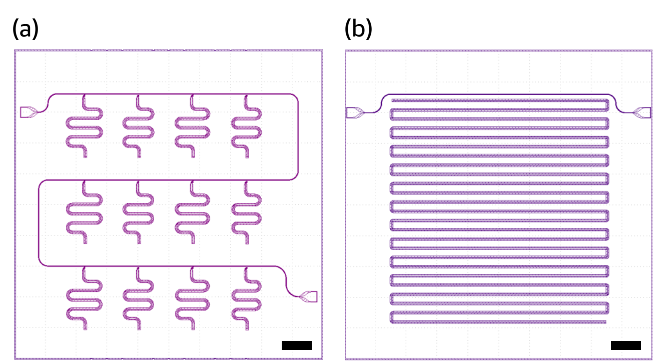

FIG. 6. (a) Quarter-wave device design. (b) Multiwavelength device design. The black scale bar at the bottom right in (a),(b) corresponds to 1 mm.

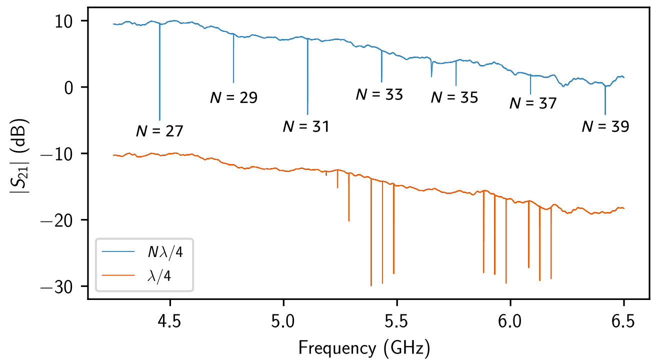

FIG. 7. Broadband S_{21} vs frequency of the $\lambda/4$ (orange) and $N\lambda/4$ (blue) resonator devices.

contained 12 $\lambda/4$ resonators inductively coupled to a common feedline in a hanger-style configuration. The multiwavelength device contained a single resonator of length 18.1 cm capacitively coupled to a feedline. The choice of inductive versus capacitive coupling does not affect the results obtained in this study.

APPENDIX B: NOMINAL RESONATOR PARAMETERS

Resonator quality factors were determined from measurements of the S_{21} scattering parameter of each device. These measurements were done with the use of a VNA in a dilution fridge setup as described in Fig. 2(c). Resonances for the $\lambda/4$ device (orange) and the $N\lambda/4$ device (blue) were identified by means of a broadband frequency sweep between 4.25 and 6.5 GHz as shown in Fig. 7; the traces have been vertically shifted for clarity.

For the $\lambda/4$ device, we identified 12 resonances dips in accordance with the 12 resonators in the device. We found that one resonator at 5.19 GHz showed unusually high power-independent loss, which was attributed to the presence of trapped flux in the ground plane near the resonator. This resonator was excluded from the study.

For the $N\lambda/4$ device, we identified seven resonances with a frequency spacing of 0.33 GHz within the 4.25–6.5 GHz range in accordance with the design. We also picked up one spurious resonance at 5.65 GHz, whose resonance frequency does not match the expected harmonics of the $N\lambda/4$ design. The presence of this extra resonance is not unexpected given that the $N\lambda/4$ resonator is more susceptible to parasitic modes due to the large division of the ground plane. The resonator quality factors extracted at high photon densities ($n_{\mathrm{ph},\lambda/4} > 10^4$) for both devices are given in Table II.

TABLE II. Quarter-wave and multiwavelength resonator frequencies and quality factors at $n_{\mathrm{ph},\lambda/4} > 10^4$.

Type	N	f_r (GHz)	Q_i ($\times 10^6$)	Q_c ($\times 10^6$)
MW	27	4.45	9.46	2.42
MW	29	4.77	2.77	2.19
MW	31	510	5.42	2.27
MW	33	5.43	3.33	2.34
MW	35	5.76	1.63	3.31
MW	37	6.08	2.20	5.40
MW	39	6.42	3.89	6.58
QW	1	5.23	1.94	3.31
QW	1	5.28	2.71	2.25
QW	1	5.39	7.53	1.79
QW	1	5.43	8.37	2.06
QW	1	5.48	6.50	1.81
QW	1	5.88	7.05	2.12
QW	1	5.93	6.83	2.04
QW	1	5.98	6.61	1.83
QW	1	6.08	4.32	2.10
QW	1	6.13	5.67	2.48
QW	1	6.18	3.97	2.06

APPENDIX C: LOSS VERSUS POWER MEASUREMENT AND DATA ANALYSIS

We used a hybrid approach to extract the power-dependent resonator loss ξ. All data presented in this appendix was taken on the $N = 33$ harmonic of the $N\lambda/4$ resonator device. We assume the S_{21} data can be modeled as

$$S_{21}(f) = e^{-j2\pi f\tau} z = e^{-j2\pi f\tau} z_\infty \frac{Q_l/Q_c e^{j\phi}}{1 + 2Q_l(f - f_r)/f_r}, \tag{C1}$$

where τ is the cable delay including the delay on the chip, z_∞ is the off-resonance point, ϕ is a mismatch angle associated with impedance mismatches in the signal chain, f_r is the resonance frequency, and Q_l and Q_c are the loaded and coupling quality factors, respectively. The intrinsic quality factor Q_i and loss ξ are subsequently calculated as

$$\frac{1}{Q_i} = \frac{1}{Q_l} - \frac{\cos\phi}{Q_c} \tag{C2}$$

$$\xi = \frac{1}{Q_i} - \frac{1}{Q_i^*}, \tag{C3}$$

where Q_i^* is the Q_i value obtained in the power-independent regime at high photon densities and represents the TLS-independent loss channels. Extraction of ξ at high photon densities can be done by fitting the data to Eq. (C1) using the conventional diameter correction method (DCM) [23]. We showcase an example DCM fit (blue line) of data (gray circles) obtained at $n_{\mathrm{ph},\lambda/4} \approx 7000$ in Fig. 8(a); note that we plot the unwrapped data $z = e^{j2\pi f\tau} S_{21}(f)$. As part of the fitting procedure, a nonlinear fit of the phase $\arg(z - z_c)$ to the function $2\arctan(2Q_l(f - f_r)/f_r) + \theta$ is performed, where z_c is the resonance circle center, f_r is the resonance frequency, and Q_l is the loaded quality factor. We show the results of this phase fit in Fig. 8(b).

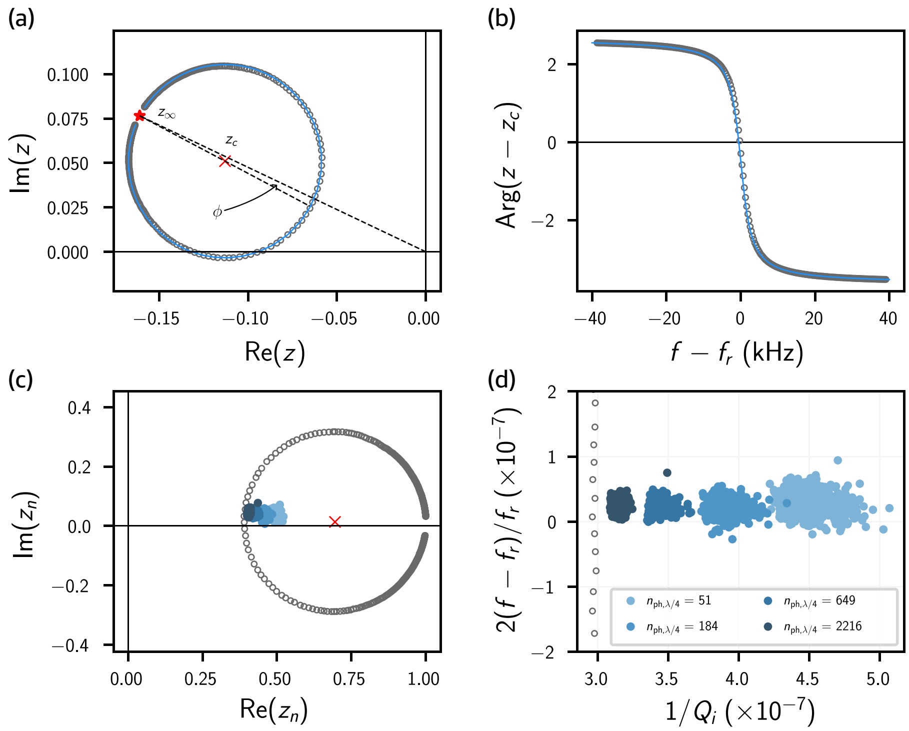

FIG. 8. Method for extracting the power-dependent loss. The data presented here were obtained on the $N = 33$ harmonic of the $N\lambda/4$ resonator device. (a) Unwrapped, frequency-dependent data z (gray circles) obtained at high photon density ($n_{\mathrm{ph},\lambda/4} \approx 7000$) plotted alongside a best fit (blue line) using the diameter correction method. Other resonator parameters used in describing the resonance circle are also shown. (b) Frequency-dependent phase of the resonance circle (gray circles) plotted alongside a best fit (blue line) to a function of the form $\arg(z - z_c) = \theta + 2\arctan(2Q_l(f - f_r)/f_r)$. (c) Normalized, high-photon-density resonance circle (gray circles) z_n plotted alongside the low-photon-density, single-frequency data obtained on resonance (blue dots). (d) With use of the power-independent resonator parameters determined at high photon density, the data shown in (c) are conformally mapped to directly obtain the resonator loss $1/Q_i$ and fractional frequency shift $2(f - f_r)/f_r$.

At photon densities approximately equal to or less than one, the SNR is reduced and the noisy data can cause the DCM fitting procedure to produce unreliable estimates of ξ. To mitigate this problem, we used the strategy outlined in Ref [15]. We collected S_{21} data at various $n_{\mathrm{ph},\lambda/4}$ values at a single frequency $f \approx f_r$. Next, we normalized the data by the off-resonance point to obtain $z_n = z/z_\infty$, which we plot as blue dots in Fig. 8(c); the normalized version of the resonance circle from Fig. 8(a) (gray circles) is also shown for reference. We proceeded to conformally map the normalized data z_n to obtain a new set of values w, whose real component Re[w] corresponded to estimates of $1/Q_i$, as we show in Fig. 8(d). The final $1/Q_i$ estimate and error were reported by our taking the mean and standard error of Re[w], which was then converted into a final estimate of ξ. This same procedure was used for the measurements taken at 200 mK.

APPENDIX D: NOISE POWER SPECTRAL DENSITY MEASUREMENT AND DATA ANALYSIS

We obtained the raw data for the PSDs shown in Figs. 4(a) and 4(b) by measuring the time-dependent $S_{21}(f, t)$ at a single frequency $f \approx f_r$ for 100 s at a sample rate of 500 Hz. To calculate the PSD in ξ, we processed the data as follows. First, we factored out the cable delay from S_{21} to obtain the unwrapped data z and then subtracted the time-averaged mean $\langle z\rangle_t$ to obtain $\delta z = z - \langle z\rangle_t$. We then projected the δz values along two constant directions,

$$\hat{r} \propto \left.\frac{\partial z}{\partial(1/Q_i)}\right|_{f=f_r}, \tag{D1}$$

$$\hat{\theta} \propto \left.\frac{\partial z}{\partial f_r}\right|_{f=f_r}, \tag{D2}$$

where $\hat{r}$ and $\hat{\theta}$ are the directions corresponding to the dissipation and frequency quadratures, respectively [22]. The projected data along the $\hat{r}$ direction were then used to calculate the corresponding PSD, $S_{\delta r}(\nu)$, according to Welch's method [28]. We used a Hann window with 50% overlap in the calculation. The final conversion to a PSD in ξ was found as

$$S_\xi(\nu) = \frac{S_{\hat{r}}(\nu)}{|\partial z/\partial(1/Q_i)|^2_{f=f_r}} = \frac{Q_c^2}{Q^4|z_\infty|^2}S_{\hat{r}}(\nu). \tag{D3}$$

TABLE III. Parameters obtained from fitting the ECDFs to a log-normal distribution.

N	f_r (GHz)	$\mu[\ln(\xi/10^{-7})]$	$\sigma[\ln(\xi/10^{-7})]$
1	5.43	1.311 ± 0.004	0.253 ± 0.006
33	5.43	1.3899 ± 0.0004	0.0442 ± 0.0006
1	6.08	1.285 ± 0.001	0.186 ± 0.002
37	6.09	1.341 ± 0.0003	0.0365 ± 0.0005

Note that we used three different frequency resolutions to plot $S_\xi(\nu)$ in Figs. 4(a) and 4(b): 0.1 Hz for $0.1\,\text{Hz} \leq \nu < 1\,\text{Hz}$, 1 Hz for $1\,\text{Hz} \leq \nu \leq 10\,\text{Hz}$, and 10 Hz for $10\,\text{Hz} \leq \nu \leq 250\,\text{Hz}$. To find the corresponding variance var[ξ], we integrated $S_\xi(\nu)$ from 0.1 to 250 Hz for each value of $n_{\text{ph},\lambda/4}$. This corresponds to a variance over a timescale of 10 s.

APPENDIX E: FITTING THE EMPIRICAL CUMULATIVE DISTRIBUTION FUNCTIONS

The ECDFs of ξ at $n_{\text{ph},\lambda/4} \sim 1$ in Figs. 5(b) and 5(d) were fitted to a log-normal distribution whose cumulative distribution function has the form

$$f(\xi) = \frac{1}{2}\left[1 + \text{erf}\left(\frac{\ln(\xi) - \mu}{\sigma\sqrt{2}}\right)\right], \tag{E1}$$

where erf is the error function, and μ and σ are the mean and standard deviation of $\ln(\xi)$, respectively. Using converted the extracted μ and σ parameters to the corresponding mean and variance of the underlying ξ as

$$E[\xi] = e^{\mu+\sigma^2/2}, \tag{E2}$$

$$\text{var}[\xi] = (e^{\sigma^2} - 1)e^{2\mu+\sigma^2}. \tag{E3}$$

We provide the results of fitting the ECDFs to Eq. (E1) in Table III.

[1] Chenlu Wang, Xuegang Li, Huikai Xu, Zhiyuan Li, Junhua Wang, Zhen Yang, Zhenyu Mi, Xuehui Liang, Tang Su, Chuhong Yang, *et al.*, Towards practical quantum computers: Transmon qubit with a lifetime approaching 0.5 milliseconds, npj Quantum Inf. **8**, 3 (2022).

[2] Olivier Ezratty, Perspective on superconducting qubit quantum computing, Eur. Phys. J. A **59**, 94 (2023).

[3] Harald Putterman, Kyungjoo Noh, Connor T. Hann, Gregory S. MacCabe, Shahriar Aghaeimeibodi, Rishi N. Patel, Menyoung Lee, William M. Jones, Hesam Moradinejad, Roberto Rodriguez, *et al.*, Hardware-efficient quantum error correction via concatenated bosonic qubits, Nature **638**, 927 (2025).

[4] Rajeev Acharya, Dmitry A. Abanin, Laleh Aghababaie-Beni, Igor Aleiner, Trond I. Andersen, Markus Ansmann, Frank Arute, Kunal Arya, Abraham Asfaw, Nikita Astrakhantsev, *et al.*, Quantum error correction below the surface code threshold, Nature **638**, 920 (2025).

[5] Clemens Müller, Jared H. Cole, and Jürgen Lisenfeld, Towards understanding two-level-systems in amorphous solids: Insights from quantum circuits, Rep. Prog. Phys. **82**, 124501 (2019).

[6] Morten Kjaergaard, Mollie E. Schwartz, Jochen Braumüller, Philip Krantz, Joel I.-J. Wang, Simon Gustavsson, and William D. Oliver, Superconducting qubits: Current state of play, Annu. Rev. Condens. Matter Phys. **11**, 369 (2020).

[7] John M. Martinis, K. B. Cooper, R. McDermott, Matthias Steffen, Markus Ansmann, K. D. Osborn, K. Cicak, Seongshik Oh, D. P. Pappas, R. W. Simmonds, and Clare C. Yu, Decoherence in Josephson qubits from dielectric loss, Phys. Rev. Lett. **95**, 210503 (2005).

[8] Jiansong Gao, Miguel Daal, Anastasios Vayonakis, Shwetank Kumar, Jonas Zmuidzinas, Bernard Sadoulet, Benjamin A. Mazin, Peter K. Day, and Henry G. Leduc, Experimental evidence for a surface distribution of two-level systems in superconducting lithographed microwave resonators, Appl. Phys. Lett. **92**, 152505 (2008).

[9] Jürgen Lisenfeld, Alexander Bilmes, Shlomi Matityahu, Sebastian Zanker, Michael Marthaler, Moshe Schechter, Gerd Schön, Alexander Shnirman, Georg Weiss, and Alexey V. Ustinov, Decoherence spectroscopy with individual two-level tunneling defects, Sci. Rep. **6**, 23786 (2016).

[10] W. Woods, G. Calusine, A. Melville, A. Sevi, E. Golden, D. K. Kim, D. Rosenberg, J. L. Yoder, and W. D. Oliver, Determining interface dielectric losses in superconducting coplanar-waveguide resonators, Phys. Rev. Appl. **12**, 014012 (2019).

[11] Conal E. Murray, Material matters in superconducting qubits, Mater. Sci. Eng.: R: Rep. **146**, 100646 (2021).

[12] Alexander P. M. Place, Lila V. H. Rodgers, Pranav Mundada, Basil M. Smitham, Mattias Fitzpatrick, Zhaoqi Leng, Anjali Premkumar, Jacob Bryon, Andrei Vrajitoarea, Sara Sussman, *et al.*, New material platform for superconducting transmon qubits with coherence times exceeding 0.3 milliseconds, Nat. Commun. **12**, 1779 (2021).

[13] C. R. H. McRae, H. Wang, J. Gao, M. R. Vissers, T. Brecht, A. Dunsworth, D. P. Pappas, and J. Mutus, Materials loss measurements using superconducting microwave resonators, Rev. Sci. Instrum. **91**, 091101 (2020).

[14] J. Gao, L. R. Vale, J. A. B. Mates, D. R. Schmidt, G. C. Hilton, K. D. Irwin, F. Mallet, M. A. Castellanos-Beltran, K. W. Lehnert, J. Zmuidzinas, and H. G. Leduc, Strongly quadrature-dependent noise in superconducting microresonators measured at the vacuum-noise limit, Appl. Phys. Lett. **98**, 232508 (2011).

[15] Cliff Chen, David Perello, Shahriar Aghaeimeibodi, Guillaume Marcaud, Ignace Jarrige, Hanho Lee, Warren Fon, Matt Matheny, and Jiansong Gao, Efficient methods for extracting superconducting resonator loss in the single-photon regime, J. Appl. Phys. **137**, 044401 (2025).

[16] Qianxu Wang, Sara Magdalena Gómez, Juan S. Salcedo-Gallo, Roy Leibovitz, Jake Freeman, Salil Bedkihal, and Mattias Fitzpatrick, Evidence of memory effects in the

dynamics of two-level system defect ensembles using broadband, cryogenic transient dielectric spectroscopy, arXiv:2505.18263 [quant-ph].

[17] W. A. Phillips, Two-level states in glasses, Rep. Prog. Phys. **50**, 1657 (1987).

[18] P. V. Klimov, J. Kelly, Z. Chen, M. Neeley, A. Megrant, B. Burkett, R. Barends, K. Arya, B. Chiaro, Yu Chen, *et al*., Fluctuations of energy-relaxation times in superconducting qubits, Phys. Rev. Lett. **121**, 090502 (2018).

[19] J. H. Béjanin, Y. Ayadi, X. Xu, C. Zhu, H. R. Mohebbi, and M. Mariantoni, Fluctuation spectroscopy of two-level systems in superconducting resonators, Phys. Rev. Appl. **18**, 034009 (2022).

[20] André Vallières, Megan E. Russell, Xinyuan You, David A. Garcia-Wetten, Dominic P. Goronzy, Mitchell J. Walker, Michael J. Bedzyk, Mark C. Hersam, Alexander Romanenko, Yao Lu, *et al*., Loss tangent fluctuations due to two-level systems in superconducting microwave resonators, Appl. Phys. Lett. **126**, 124001 (2025).

[21] C. T. Earnest, J. H. Béjanin, T. G. McConkey, E. A. Peters, A. Korinek, H. Yuan, and M. Mariantoni, Substrate surface engineering for high-quality silicon/aluminum superconducting resonators, Supercond. Sci. Technol. **31**, 125013 (2018).

[22] Jiansong Gao, The Physics of Superconducting Microwave Resonators, Ph.D. thesis, California Institute of Technology, 2008, https://resolver.caltech.edu/CaltechETD:etd-06092008-235549.

[23] M. S. Khalil, M. J. A. Stoutimore, F. C. Wellstood, and K. D. Osborn, An analysis method for asymmetric resonator transmission applied to superconducting devices, J. Appl. Phys. **111**, 054510 (2012).

[24] W. A. Phillips, *Amorphous Solids* (Springer-Verlag, New York, 1981).

[25] Lara Faoro and Lev B. Ioffe, Interacting tunneling model for two-level systems in amorphous materials and its predictions for their dephasing and noise in superconducting microresonators, Phys. Rev. B **91**, 014201 (2015).

[26] J. Gao, J. Zmuidzinas, A. Vayonakis, P. Day, B. Mazin, and H. Leduc, Equivalence of the effects on the complex conductivity of superconductor due to temperature change and external pair breaking, J. Low Temp. Phys. **151**, 557 (2008).

[27] C. Neill, A. Megrant, R. Barends, Yu Chen, B. Chiaro, J. Kelly, J. Y. Mutus, P. J. J. O'Malley, D. Sank, J. Wenner, *et al*., Fluctuations from edge defects in superconducting resonators, Appl. Phys. Lett. **103**, 072601 (2013).

[28] P. Welch, The use of fast Fourier transform for the estimation of power spectra: A method based on time averaging over short, modified periodograms, IEEE Trans. Audio Electroacoust. **15**, 70 (1967).

[29] A. Dvoretzky, J. Kiefer, and J. Wolfowitz, Asymptotic minimax character of the sample distribution function and of the classical multinomial estimator, Ann. Math. Stat. **27**, 642 (1956).

[30] Tamin Tai, Jingnan Cai, and Steven M. Anlage, Anomalous loss reduction below two-level system saturation in aluminum superconducting resonators, Adv. Quantum Technol. **7**, 2200145 (2024).

[31] Paul Szypryt, Development of Microwave Kinetic Inductance Detectors for Applications in Optical to Near-IR Astronomy, Ph.D. thesis, University of California Santa Barbara, 2017.

[32] Cliff Chen, Shahriar Aghaeimeibodi, Yuki Sato, Matthew H. Matheny, Oskar Painter, and Jiansong Gao, Supporting data for "Broadband high-precision measurement of two-level-system loss using multi wavelength superconducting resonators" (2025), https://doi.org/10.6084/m9.figshare.30193276.v1.